Joint inversion of broadband teleseismic and interferometric synthetic aperture radar (InSAR) data for the slip history of the Mw=7.7, Nazca ridge (Peru) earthquake of 12 November 1996

J. Salichon, B. Delouis, P. Lundgren, D. Giardini, M. Costantini, P. Rosen

Joint inversion of broadband teleseismic and interferometric synthetic aperture radar (InSAR) data for the slip history of the Mw = 7.7, Nazca ridge (Peru) earthquake of 12 November 1996

J. Salichon,[1] B. Delouis,[1,2] P. Lundgren,[3] D. Giardini,[1] M. Costantini,[4] and P. Rosen[3]

Received 10 August 2001; revised 16 July 2002; accepted 8 November 2002; published 8 February 2003.

[1] The slip distribution of the 12 November 1996, Mw = 7.7, Peru earthquake is determined using broadband teleseismic waveforms, a differential SAR interferogram (interferometric synthetic aperture radar [InSAR]), and a fault parametrization allowing slip and rupture velocity to vary along the rupture plane. Both data sets are inverted jointly to limit the trade-off between the space and time aspects of the rupture. The earthquake fault plane is located at the subduction interface; it strikes parallel to the trench and dips 30° NE. By inverting synthetic data, we show how the InSAR and teleseismic data are complementary and how the joint inversion produces a gain in the spatial and temporal resolution of the slip model, even with a SAR interferogram that covers only part of the coseismic deformation. The rupture of the 1996 Peru event initiated on the southern flank of the subducted Nazca ridge and propagated unilaterally toward the southeast (along strike) for more than 100 km at a depth between 20 and 40 km. The area of maximum slip (6–7 m) is located 50 km southeast of the hypocenter. The total seismic moment is 4.4×10^{20} N m (our joint inversion). The source time function is approximately 60 s long and presents three major pulses of moment release. The dominant one, which occurred between 30 and 45 s, does not correspond to the area of largest slip but to the rupture of a wide zone located about 100 km away from the hypocenter where slip reaches only 2–3 m. Computed coseismic coastal uplift correlates well with the location of raised marine terraces and with the topography of the coastal cordillera, suggesting that these features may be related to the repetition of 1996-type events at the interface between the Nazca ridge and the South American plate. *INDEX TERMS:* 1242 Geodesy and Gravity: Seismic deformations (7205); 7205 Seismology: Continental crust (1242); 7215 Seismology: Earthquake parameters

Citation: Salichon, J., B. Delouis, P. Lundgren, D. Giardini, M. Costantini, and P. Rosen, Joint inversion of broadband teleseismic and interferometric synthetic aperture radar (InSAR) data for the slip history of the Mw = 7.7, Nazca ridge (Peru) earthquake of 12 November 1996, *J. Geophys. Res.*, *108*(B2), 2085, doi:10.1029/2001JB000913, 2003.

1. Introduction

[2] In the past decades, considerable effort has been dedicated to the study of the rupture process of large earthquakes using seismic and geodetic data. One of the main outcomes of those studies is that the slip distribution associated with large earthquakes is generally heterogeneous. Understanding the space and time characteristics of large ruptures is particulary important for the study of earthquake dynamics, the earthquake cycle, and the assessment of seismic hazard. Traditionally, teleseismic P- and S-wave pulses have been used to image the rupture history in terms of total source time function, slip map and local slip-rate. However, the ability to resolve the details of the rupture depends strongly on type of data used, on the inversion algorithm and of course on the degree of complexity of the source itself. Broadband seismic data may not be sufficient for a unique and reliable mapping. A way to deal with this problem is to derive rupture models by matching different data sets which include multiple constraints from independent observations, such as strong motion, GPS, remote sensing and surface breaks [*Wald and Heaton*, 1994; *Hernandez et al.*, 1999; *Wright et al.*, 1999]. We combine two independent data sets acquired at remote distances, far-field teleseismic P and SH waves and near-source synthetic aperture radar (SAR) interferometric data. The geodetic interferometric synthetic aperture radar (InSAR) data obtained from the ERS1/2 satellites can sample surface deformation over a large area around the earthquake, and provide constraint on the slip distribution that is totally independent from the rupture timing. In our joint inversion scheme, we fit simultaneously the waveforms and the geodetic data, in order to reduce the possible

[1]Institute of Geophysics, Eidgenossische Technische Hochschule, Zurich, Switzerland.
[2]Now at Geosciences Azur, CNRS/UNSA, Nice-Sophia Antipolis, France.
[3]Jet Propulsion Laboratory, Pasadena, California, USA.
[4]Telespazio, Rome, Italy.

0148-0227/03/2001JB000913$09.00

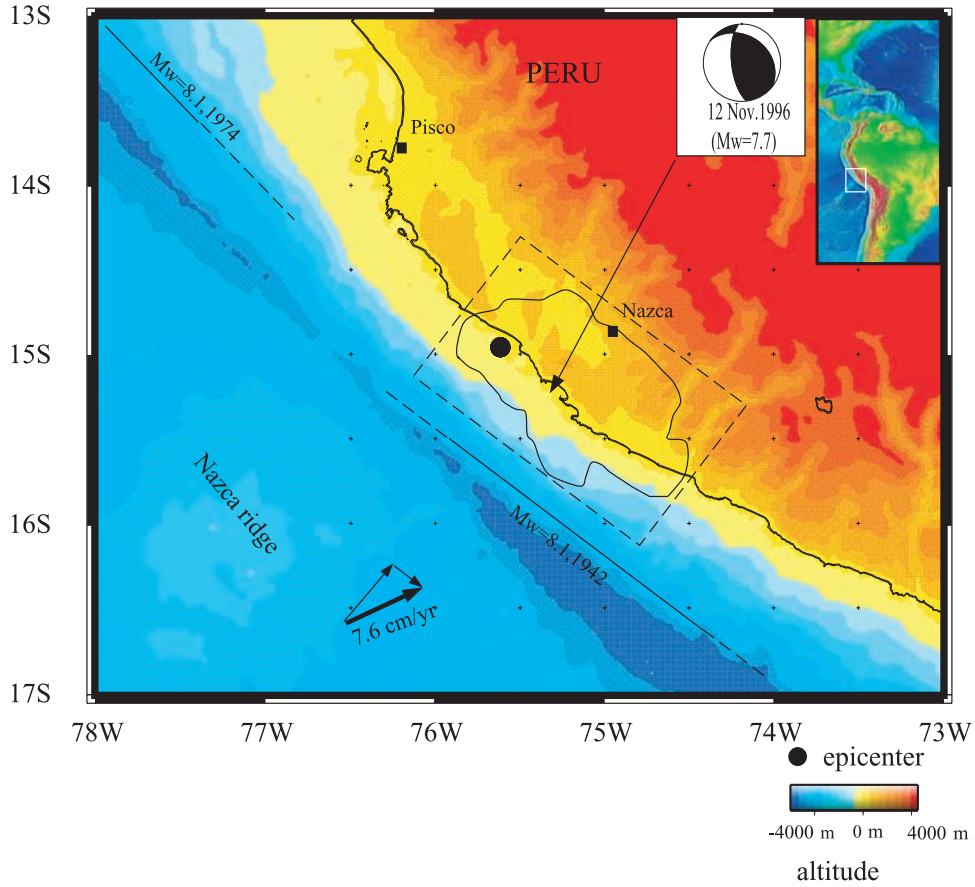

Figure 1. Location of the Mw = 7.7, 12 November 1996, Peru earthquake in front of the Nazca ridge. The position of the epicenter is indicated by the black dot. The dashed rectangle shows the surface projection of the fault plane model (this study) and the shaded area the extent of the rupture area obtained from the joint inversion of teleseismic and InSAR data. Also indicated is the Harvard CMT focal mechanism (Mo = 4.57 10^{20} N m), the rupture zone of the 1942, Mw = 8.2. earthquake and the southern extent of the Mw = 8.1, 3 October 1974, earthquake [*Dorbath et al*, 1990]. The arrow indicates the relative velocity between the Nazca and the South American plates (7.6 cm/yr).

trade-off between rupture timing and slip location, and therefore to enhance the reliabilty of the resulting slip distribution. A similar approach has been successfully applied to the 1999, Izmit (Turkey), Mw = 7.6 earthquake [*Delouis et al.*, 2000, 2002], where broadband, InSAR, GPS, strong motion and surface break data have been combined in a single inversion scheme, allowing the exploration of the resolving power of the individual data sets. The 12 November 1996, Mw = 7.7, Peru-Nazca ridge earthquake is one of the first large subduction earthquakes whose surface deformation has been mapped by ERS1/2 satellites. This thrust event had a large extent, mostly offshore. The ERS1/2 satellites measurements monitored the entire onshore coseismic ground deformation. Despite the large coverage of the event, the precise Digital Elevation Model needed to process the final differential interferogram could be obtained only for a limited area, restricting the geodetic control to the southern extent of the deformation field. Nevertheless, the inversions of the separate and combined data sets are of interrest to analyze how a partial control from remote sensing can complement the teleseismic data to map the source complexity in a remote location where no others data were available and where typically no surface breaks can be observed. Synthetic tests are carried out to assess the benefits of the joint inversion. They contribute to demonstrate the major improvements in the space and time resolution of slip that can be expected in the joint inversion of real teleseismic and InSAR data.

2. The 1996 Peru Earthquake

[3] The 12 November 1996, Mw = 7.7, Peru earthquake occurred at the subduction interface between the Nazca ridge and the South American plate (Figure 1). It caused human losses and building damages, landslides within about 200 km of the epicenter, as well as coastal uplift [*Chatelain et al.*, 1997]. The mechanism corresponded to underthrusting, as indicated by the Harvard CMT solution (strike 312°, dip 33° and rake 55°). The epicenter has been relocated by *Spence et al.* [1999], offshore near the coast of Peru, at 14.99°S and 75.63°W. This event occurred in the vicinity of the former Mw = 8.1, 24 August 1942 epicenter and it has already been proposed that the 1996 and 1942 ruptures overlapped, at least partially, both events being located in front of the southern side of the subducting Nazca ridge [*Spence et al.*, 1999; *Swenson and Beck*, 1999]. Other recent

Table 1. ESA Precision Orbits (PRC)

Satellite	Track	Orbit	Date
ERS1	39	5194	19920713
ERS2	39	12919	19971009
ERS1	39	27582	19961023
ERS2	39	7909	19961024

large earthquakes took place further north of the Nazca ridge and the subduction interface between the rupture areas of the 1996, 1942 events and that of the 3 October 1974 earthquake appears to be unbroken for several centuries [*Kelleher*, 1972; *Dorbath et al.*, 1990; *Swenson and Beck*, 1999]. The Nazca ridge is an aseismic and volcanic bathymetric high, an area of elevated crust about 200 km wide, located on the oceanic Nazca plate. Consumption of the Nazca ridge at the convergent boundary (7.6 cm/yr) migrates southeastwardly along the coast due to its oblique orientation with respect to the trench [*Hsu*, 1992]. The subduction of such a buoyant structure is still poorly understood and an accurate retrieval of the slip history would shed light on the relationship between the ridge and the South American plate in this area.

3. InSAR and Teleseismic Data

[4] The raw differential interferogram was generated using two pairs of ERS1/2 scenes and the ESA precision orbits (PRC) (Table 1). We used a four-pass technique to process the data with the ROI-PAC software developed at the Jet Propulsion Laboratory and Caltech. The topography has been generated from a first pair of interferograms, the 1996-10-23 (ERS-1) and 1996-10-24 (ERS-2) raw tandem scenes. This has been flattened and unwrapped with the minimum cost flow algorithm of *Costantini* [1998]. It was then unflattened (i.e. the Earth curvature added back) and the differential interferogram formed from a second coregistered change pair interferograms (1992-07-13 and 1997-10-09) representing a time delay of four years before and one year after the event. Figure 2a shows the observed interferogram where displacements are represented with a 5 cm fringe cycle by interpolation on the original unwrapped interferogram with 2.8 cm fringe cycle. The northernmost fringes are unexpected and are possibly due to baseline errors which could produce a phase ramp, although the baselines were reestimated based on the amplitude offsets in the single look complex images. However, the significant elevation change along track (0–5000 m) limits our ability to accurately refine the baseline from the amplitude data alone. The phase ramp is largest in the azimuthal direction (along satellite track), and should be corrected for. Nonetheless, we can recognize the central area of subsidence associated with the thrust event (closed fringes in the lower half of the interferogram) and part of the uplift zone indicated by the high fringe rate observed near the coast, and confirmed by observations of coastal uplift [*Ocola et al.*, 1997; *Chatelain et al.*, 1997]. The contribution of aftershocks to the final static ground displacement is not considered since the largest aftershocks are located mostly offshore and are several orders of magnitude smaller than the main shock [*Spence et al.*, 1999]. We assume that the differential interferogram represents essentially the coseismic deformation. Nevertheless, in the absence of additional data we cannot rule out some postseimic contributions in the period from 12 November 1996 to 10 October 1997. For the inversions, we use a set of 1213 georeferenced points distributed over the whole interferogram, denser where the gradient in the ground displacements is larger (Figure 2b).

[5] Seismological data have been collected through the IRIS and Geoscope networks. They consist of P and SH seismograms recorded at teleseismic distances. Seismic records have been deconvolved from the instrument response and integrated to obtain ground displacement. The seismograms have been bandpassed from 0.8 Hz (P waves) or 0.4 Hz (Sh-waves) to 0.01 Hz. We model the first 90 s of 13 P waves signals and the first 120 s of 11 SH-waves signals well distributed in azimuth around the source.

4. Fault Model and Inversion Procedure

[6] Preliminary estimates of the fault strike, dip and rake, as well as the hypocentral depth were obtained from broadband teleseismic modeling using the method of *Nabelek* [1984]. Values for those parameters were confirmed or adjusted by trial and error inversions performed with both the InSAR and teleseismic data. The rupture is parametrized by a fault plane aligned with the Peru trench, striking 307° and dipping 30° to the northeast. The center of the fault and the hypocenter are located at 33 km along strike and at 28 km depth respectively (Figure 3). The dimensions of the fault model are 180 km along strike and 120 km along dip. It is subdivided into 54 subfaults with dimensions of 20 by 20 km2. For each subfault strike and dip are held fixed. Their respective slip angle (rake) is allowed to vary independently from the neighbor subfaults within the range 50 ±15° (reverse-sinistral faulting). The inversion procedure follows the approach of *Delouis et al.* [2000]. The subfault slip rate functions are based on the parametrization of the source function from *Nabelek* [1984] and represented by a sequence of 4 isoscele triangular time windows of variable height, mutually overlapping, each having a duration of 5 s and spaced by 2.5 s. The maximum duration of slip on a subfault is thus 12.5 s. A longer duration does not produce measurable changes in the modeling. The maximum allowed slip on each subfault is 7 m and we verified that a higher bound for the maximum slip did not improve the modeling. Nevertheless, by limiting the maximum slip we favor smoother slip distributions. The rupture initiates at the hypocenter and propagation is represented by the subfault rupture onset times that are allowed to vary within the range defined by two bounding rupture velocities, 1.8 and 3.5 km/s. We assume a simple half-space crustal model with Vp = 6.6 km/s and Vs = 3.8 km/s. We solve for the following free parameters at each subfault: the rupture onset time, the amplitudes of the four elementary triangular time windows, and the rake.

[7] Furthermore, we invert for one static offset to calibrate the InSAR data since the differential interferograms provide only a relative measurement of the deformation and the actual location of the ''zero displacement fringe'' is unknown. Due to the baseline errors accounting for a phase ramp along the track direction (azimuth −166°) shown by the additional fringes perpendicular to the satellite track in the northern part (Figure 2a), two more free parameters have to be introduced in the inversion of InSAR data: the position

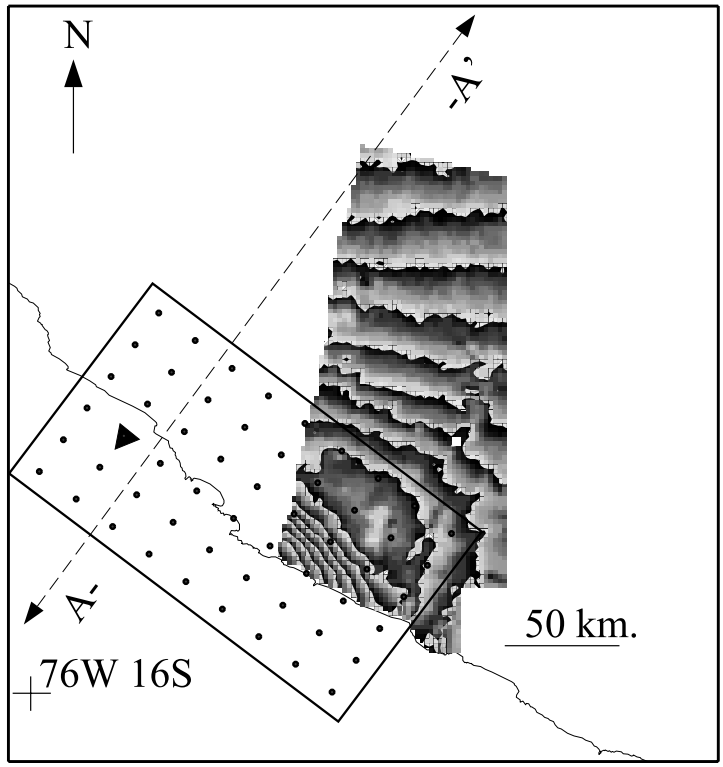

a)

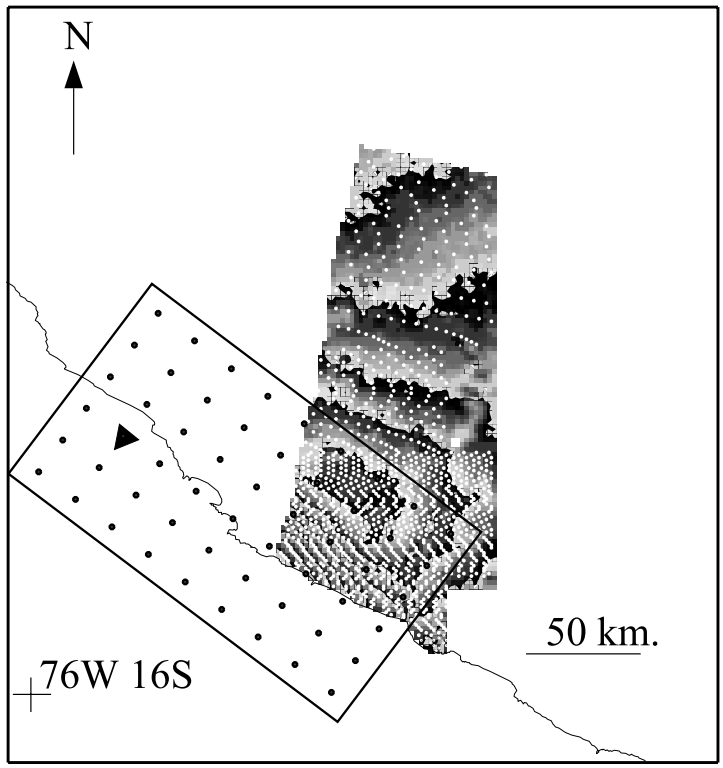

b)

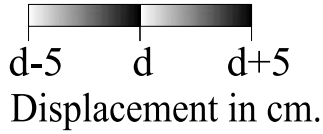

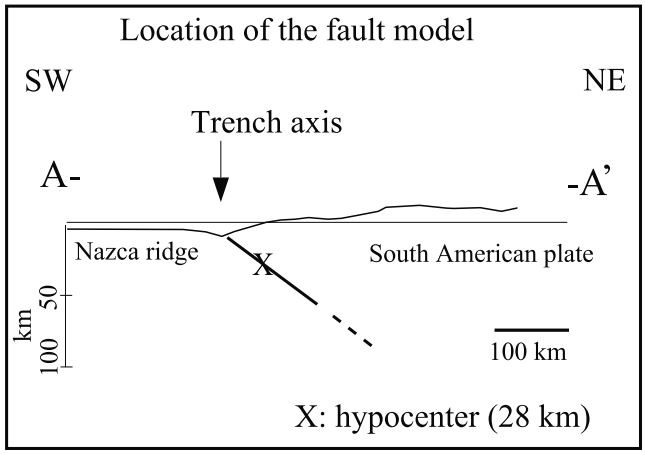

Figure 3. Topographic cross section A–A′ of Figure 2, with the position the fault plane model (thick line).

along track of the ramp axis and the ramp slope. These are inverted using the InSAR data only and then kept fixed in the joint inversion (Figure 2b). The displacement values are corrected (increased or decreased) depending on their location with respect to the ramp axis location. The static near-source ground displacement is modeled using the dislocation formulation of *Savage* [1980]. Each subfault is represented by a dislocation surface embedded in an elastic half-space.

[8] The synthetic seismograms produced by simple shear dislocations (double couple) point sources at the center of each subfault, are computed using the ray theory for stations located at teleseismic distances [*Nabelek*, 1984]. The inversion is performed with a simulated annealing algorithm that allows for a quasi-global exploration of the model space. The primary cost function is the root mean square (RMS) error of the data fit normalized by the observed data. Both data sets have unit weight in the joint inversion. We consider that an appropriate weighting of the different data sets in the joint inversion should distribute the slight degradation of the data fit (with respect to the separate inversions) quite evenly on the different data sets. Since both the InSAR and the teleseismic data remain correctly fitted with equal weights in the joint inversion, we deem that the importance of both data sets is well balanced for unit weights. An additional cost function is used in the InSAR and joint inversions to penalize solutions with seismic moments higher than a reference moment which is the Harvard Centroid Moment Tensor (HCMT) in the case of real data. This is particularly important since slip on subfaults located far from the InSAR data points may be easily overestimated.

5. Resolution Tests With Synthetic Data

[9] We investigate the space-time resolving power of the different data sets using synthetic slip maps, giving a special attention to the impact of an incomplete coverage of the displacement field from the InSAR data. The data processing and fault model are the same as in the inversions of the actual data. The number of free parameters, their bounding values, and the moment minimization are also kept identical to those that are used for the Peru event.

[10] The synthetic data (Figures 4–5) are generated with a five patches model (Figure 6a). A low level of random noise has been added to the data in order to include small deviations from the exact solutions: maximum ±1 cm on the InSAR data (compared to the 2.8 cm of the ERS1/2 radar wavelength) and a modification of ±10% on the amplitudes of the teleseismic data also randomly time-shifted by a maximum of ±1s. The synthetic slip map is composed by five asperities, each comprising four subfaults slipping 170 cm, plus 40 cm of slip at the hypocenter. Rake is 50° everywhere. The total scalar seismic moment is 5.57×10^{20} N m. Rupture velocity is constant and equal to 2.7 km/s. All the elementary source time functions have the same amplitude. The rupture initiates at the same hypocenter location as for the actual earthquake.

[11] We examine the resolving power for the teleseismic, InSAR, and combined data sets. Two different coverages of the synthetic InSAR data are considered (Figure 4): one corresponds to the actual coverage (called ''narrow''), and the other takes into account most of the inland ground displacement (called ''wide''). The synthetic InSAR and joint inversions are performed for those two distributions.

[12] Table 2 displays the RMS and scalar seismic moment resulting from the inversions. No moment minimization is used in the teleseismic inversion since the seismic moment remains in any case lower than the reference moment of the synthetic model. The resulting slip maps are presented on Figure 6.

[13] When inverted alone, the teleseismic data tend to spread out slip over the entire fault plane (Figure 6b). The asperities are nonetheless quite well resolved at the beginning of the rupture, in the vicinity of the hypocenter, but imaging deteriorates in the later SE part. This shows the difficulty to model the latest parts of the P and SH pulses when all the contributions from the source overlap in the teleseismic signals. Furthermore in the real case, the P and SH pulses are disturbed by the contribution of crustal complexities which are not taken into account in our tests.

[14] The separate InSAR data inversions (Figure 6c–6d) give more accurate locations of the slip patches, but with the actual ''narrow'' coverage, the NW part of the rupture, around the hypocenter, is not properly retrieved, and slip at the NW bottom corner of the rupture is largely overestimated. This is related to the decreasing resolving power of geodetic data with distance to the subfaults. With the ''wide'' coverage of InSAR data, resolution improves, especially in the NW part. The joint inversions (Figure 6e–6f) combine the resolutions of the separate teleseismic and InSAR inversions, and retrieve the slip maps more completely and accurately.

Figure 2. (opposite) Location of the InSAR data and surface projection of the fault plane model. The epicenter is indicated by the black triangle while the small dots correspond to the centers of the subfaults. Each fringe (black-gray-white gradation) corresponds to 5 cm of displacement in the direction toward the satellite. (a) Raw differential interferogram represented here with a 5 cm fringe cycle. (b) Interferogram corrected with the phase ramp. White points represented on the interferogram are the data points used for the inversions.

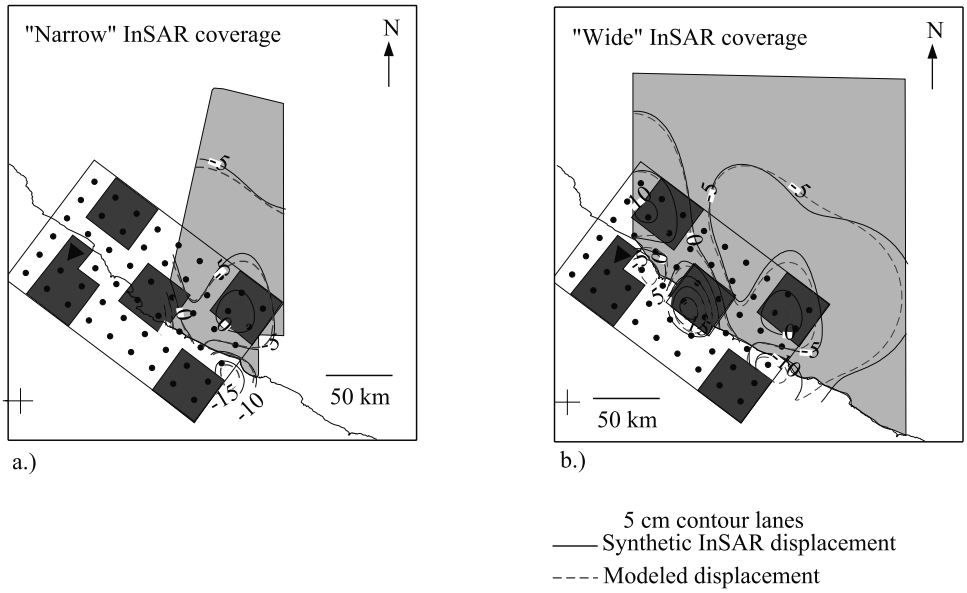

Figure 4. Surface projection of the synthetic fault model with five slip patches (dark gray areas) used for the resolution tests together with the synthetic and inverted InSAR data. The light gray areas correspond to the "narrow" (left) and "wide" (right) coverages of InSAR data. The contour lines are drawn every 5 cm of ground displacement in the satellite line of sight. Modeled means from the joint inversions.

[15] The resolution of timing has also been assessed (Figure 7). Although all the inversions that incorporate the teleseismic data provide a good estimate of the rupture velocity, combining the two data sets (joint inversion) helps to retrieve the patches at the end of the rupture with the correct timing (hypocentral distance >100 km, SE half of the fault plane). This confirms that the trade-off between rupture timing and slip location that affects seismological data inversions can be reduced through the addition of geodetic data.

6. Inversion Results

[16] The results of the separate and joint inversions of the real data sets are presented in Figures 8–10 (data modeling), and 11 (slip maps). The fit of the geodetic data (Figure 8) is good for both the InSAR and joint inversions, though it degrades slightly in the north with distance from the fault. Misfit does not exceed 5 cm in both cases. modeling of the teleseismic data in the separate and joint inversions are similar and there is no systematic misfit (Figures 9–10). As in the case of the synthetic tests, the teleseismic data tend to underestimate the seismic moment if compared to the HCMT moment (4.57×10^{20} N m). Table 3 displays the RMS values for the inversions and shows that fit degrades only slightly when data are combined.

[17] The slip distributions (Figure 11) show common features along strike. The rupture propagated to the SE of the hypocenter. In preliminary inversions, we tested fault models extending more toward the NW but data do not require it.

[18] In the teleseismic inversion, two areas of higher slip are found, one at the hypocenter and the other about 50 km more to the SE along strike. The InSAR inversion does not retrieve any slip in the vicinity of the hypocenter, as expected from the resolution tests. The region of main slip (up to 680 cm) is located at about 50 km of the hypocenter to the SE and slightly downdip. Significant slip occurs also farther to the SE along strike.

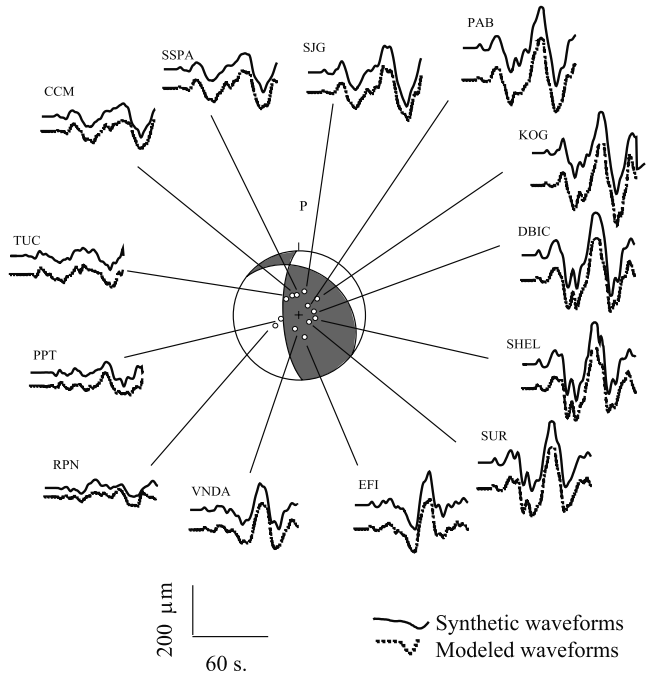

Figure 5. Focal mechanism and P waveforms modeling from the joint inversion with the synthetic 5 patches slip model and the "narrow" InSAR coverage.

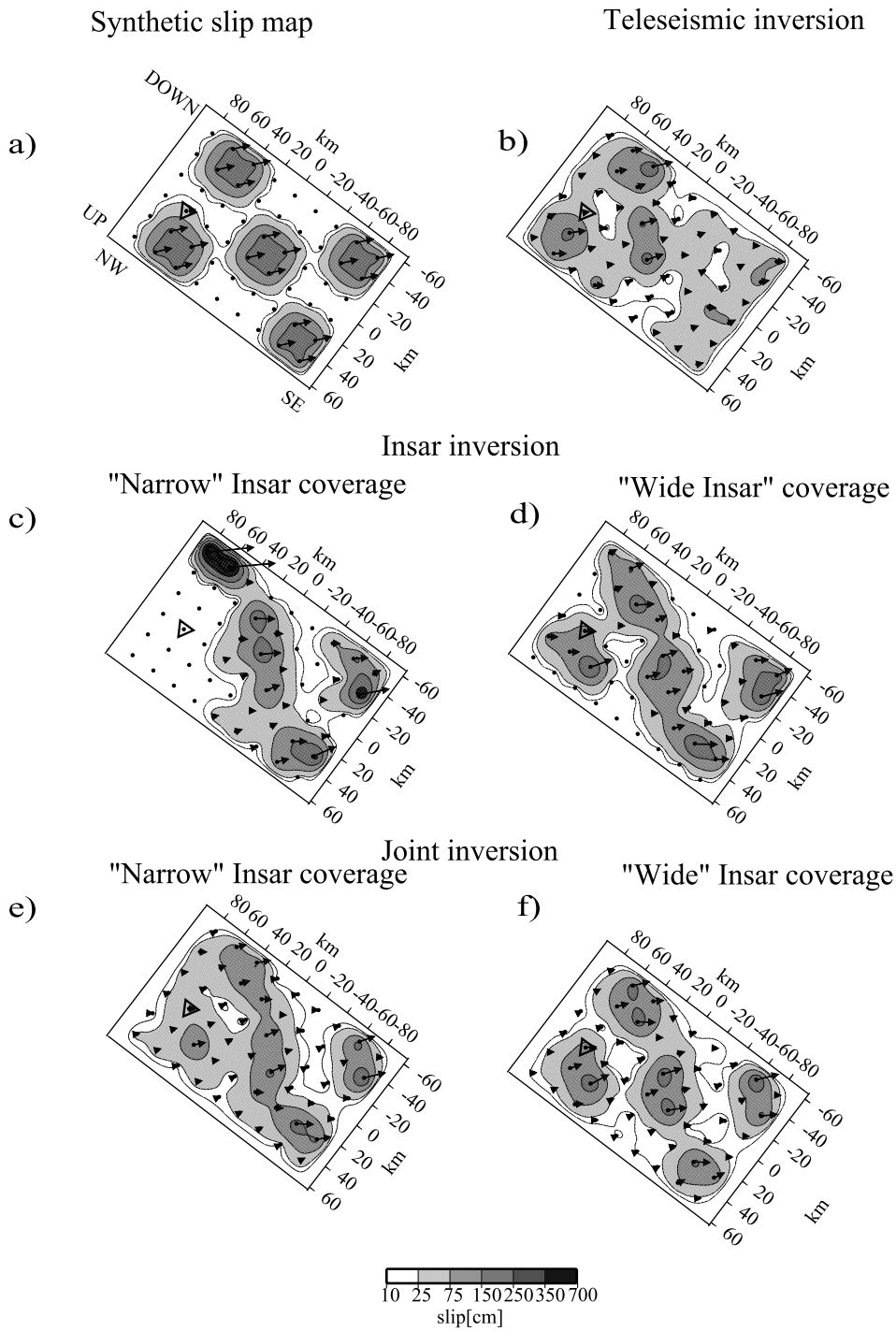

Figure 6. Slip maps from the resolution tests. The centers of the subfaults are shown by the dots, the epicenter by a triangle. Rakes are shown by arrows whose length is proportional to slip and which indicate the underthrusting direction.

[19] The joint inversion combines the characteristics of the previous separate inversions: slip at the hypocenter, maximum slip 50 km SE of it, and still large slip 50 km further to the SE, i.e. 100 km away from the hypocenter. A slip area previously found downdip (−40 km , −30 km on the fault plane) in the InSAR inversion is now translated updip to a neighbor subfault. The resolving power of the data is not sufficient to discriminate between these two neighbor locations for the peak slip. In all, the main slip area is about 100 km long with most of slip restricted to a 60 km wide strip along strike in the depth range 20 to 40 km depth.

[20] The time evolution of the rupture from the joint inversion is presented in Figure 12 with the corresponding overall source time function (STF). Rupture extends unilaterally along strike, i.e. from NW to SE, in about 60 s. The

Table 2. Misfit Values and Scalar Seismic Moment Resulting From the Inversions of the Synthetic Data[a]

		InSAR		Joint	
	Teleseismic	"Narrow"	"Wide"	"Narrow"	"Wide"
RMS teleseismic data	0.163	-	-	0.20	0.20
RMS InSAR data	-	0.1	0.1	0.16	0.17
Moment (10^{20} N m)	4.82	5.63	5.37	4.9	4.9

[a]Reference moment = 5.67×10^{20} N m.

STF displays three main pulses of energy: The first one, between 0 and 10 s corresponds to the rupture of the hypocentral asperity. The second centered at 22 s is associated with the breaking of the asperity that is found with the highest slip value. The third and major one, between 30 and 45 s, involves a very large area of slip in the SE half of the rupture.

7. Slip Models and Previous Studies of the 1996 Peru Earthquake

[21] Previously, the rupture history of the 1996 Nazca ridge earthquake has been studied using teleseismic data by *Swenson and Beck* [1999], and by *Spence et al.* [1999]. In Figure 13, we compare the different inversion results. All studies show rupture propagation toward the SE but the results differ in the estimation of the seismic moment and in the details of the slip distribution. Comparison of *Swenson and Beck* [1999] and *Spence et al.* [1999] shows that teleseismic data may be explained by seismic moments varying by a factor 4 or more (3.47×10^{20} to 1.5×10^{21} N m). These previous studies locate the maximum energy release (Swenson and Beck) or the main slip patch (Spence et al.) about 100 km to the SE of the hypocenter, where we also find the main contribution of slip and maximum moment release in the source time function (Figure 12). However, we find that the main asperity is located only 50 km to the SE of the hypocenter. In addition to be controlled by the teleseismic data, this location is also constrained by the InSAR data in our study.

8. Relation Between the 1996 Earthquake and the Coastal Deformation

[22] As mentioned before, the Mw = 7.7, 12 November 1996, and the Mw = 8.1, 24 August 1942, events damaged the same region [*Chatelain et al.*, 1997] which displays a characteristic feature (Figure 14a): a narrow uplifted coastal cordillera reaching 1000 m within the peruvian fore-arc, in front of the Nazca ridge [*Hsu*, 1992; *Machare and Ortlieb*, 1992]. The probable repetition of such earthquakes at the subduction interface of the Nazca ridge, may have some

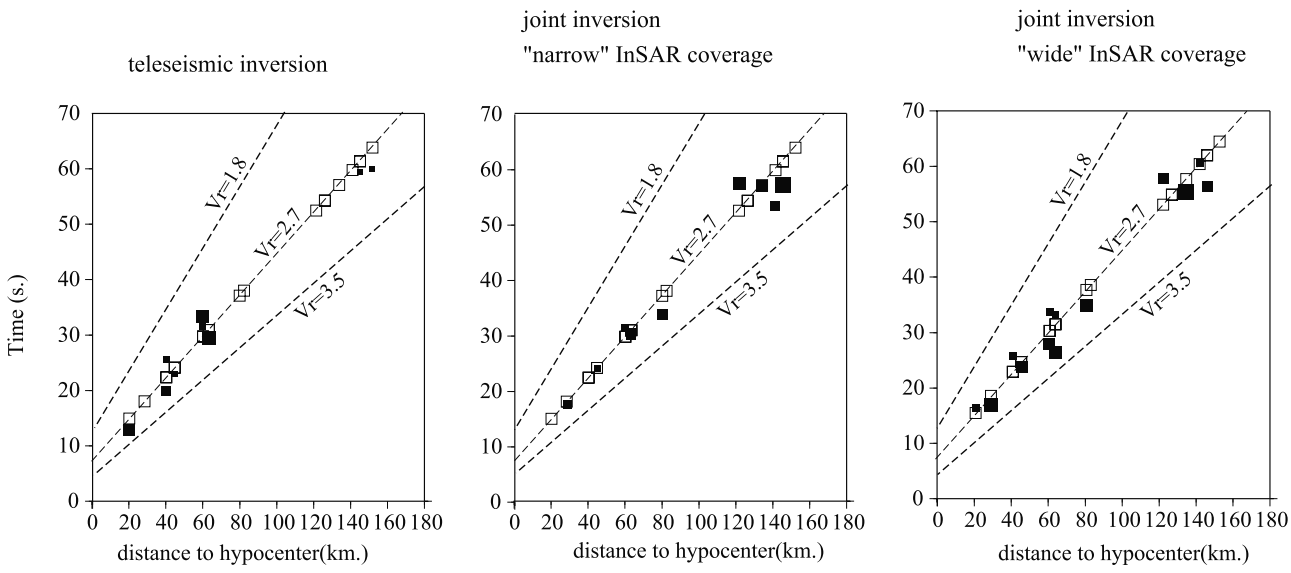

Figure 7. Timing of the rupture on the subfaults versus the distance to the hypocenter. Rupture timing of the subfaults from the reference model is represented by the empty squares. Black filled squares represent inversion results for subfaults whose location coincide with the synthetic slip patches and whose slip amplitude reaches at least half of the reference slip. Square size is proportionnal to the total slip of the subfault. Also shown are the maximum and minimum rupture time lines defined by the rupture velocities (vr) 1.8 and 3.5 km/s respectively. The minimum slip duration corresponds there to a single time window (5 s) and the maximum slip duration to 4 overlapping windows (12.5 s). The light dashed line represents the reference timing for a rupture velocity of 2.7 km/s.

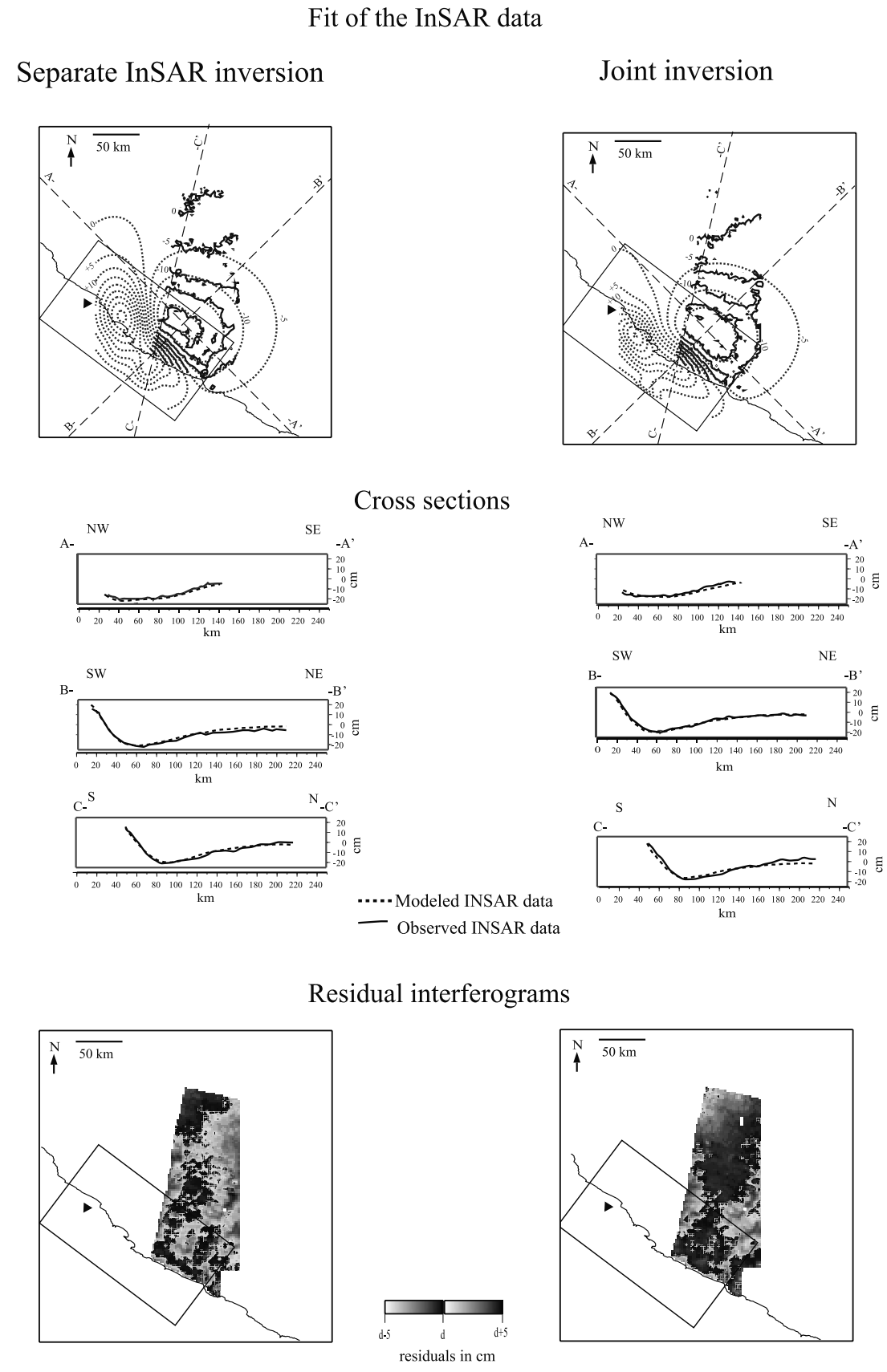

Figure 8. Fit of the InSAR data for separate InSAR (left) and joint inversion (right). The observed displacement contour lines (corrected from the static offset) are shown in blue. The modeled InSAR data are shown in red. Three cross sections show how well the data are fit. The residual interferograms formed by the difference between observed and modeled data are displayed at the bottom.

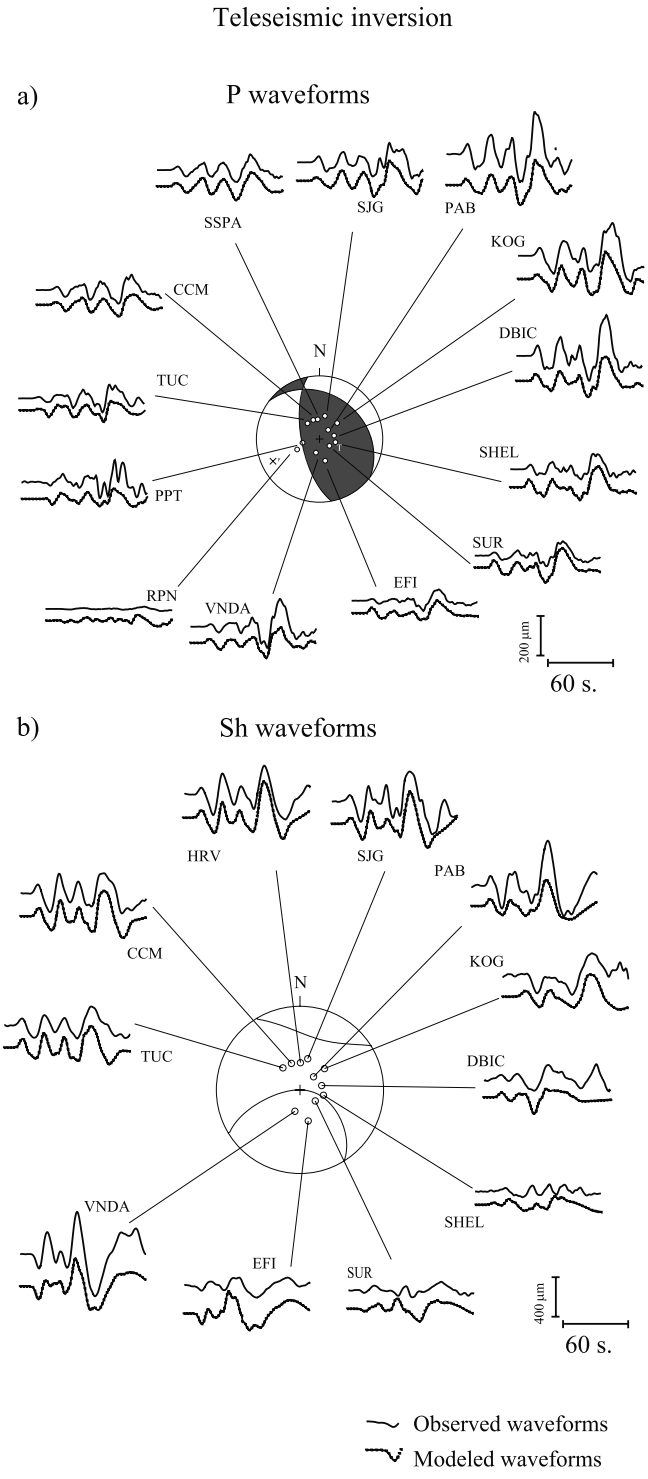

Figure 9. Average focal mechanisms of the P and SH waves determined by the teleseismic inversion, and the waveform fitting.

tectonic implications and imaging precisely the distribution of slip for the last Peru event is essential to shed light on the contribution of those earthquakes to the coastal uplift of the fore-arc relief. A similar situation has also been proposed where an aseismic ridge is subducted under Costa Rica [*Marshall and Anderson*, 1995].

[23] We computed the vertical displacement at the surface due to our preferred earthquake model and compared it to the main geomorphological features of the coastal area [*Machare and Ortlieb*, 1992]. The resulting vertical bulge is mostly located offshore and elongated about 200 km along strike (Figure 14a). It presents a maximum uplift (>50 cm) above the area of maximum slip on the fault plane. Onshore, the uplift involves the southeastern part of the Pisco basin region where the vertical displacement occurs mainly along coast in the coastal cordillera region. The profile of coseismic uplift along the coast is very similar to the topographic profile of the coastal cordillera, to the elevation of the uplifted marine terraces [*Hsu*, 1992; *Machare and Ortlieb*, 1992], and to the bathymetric cross section of the Nazca ridge (Figure 14b). We propose that the

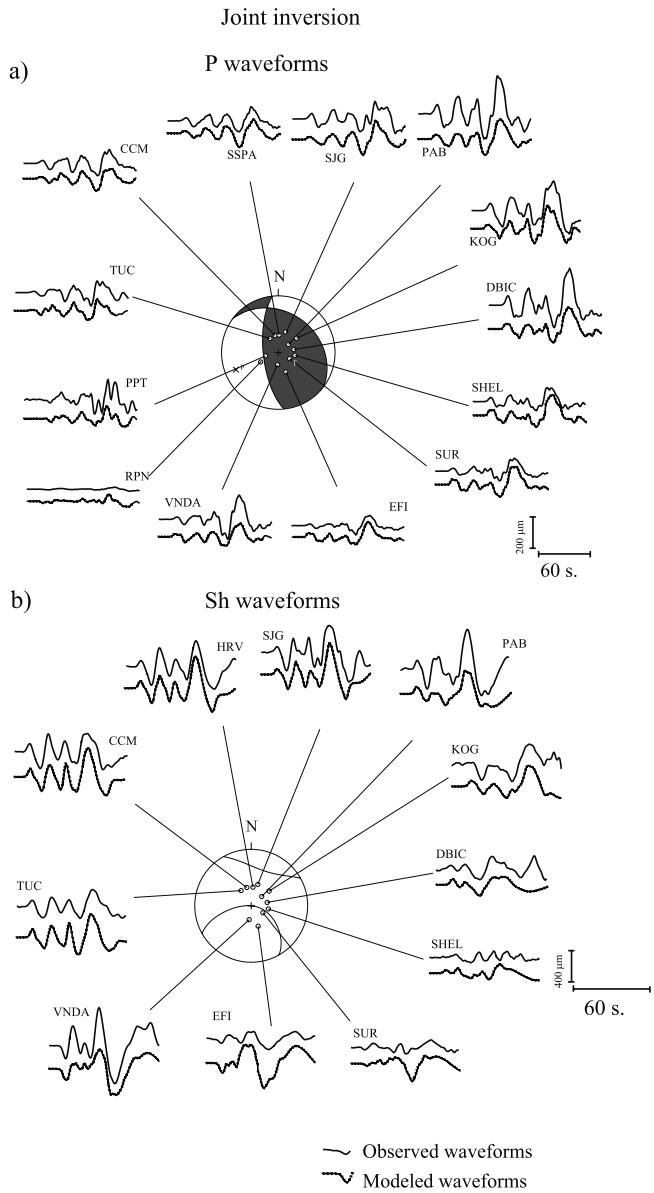

Figure 10. Average focal mechanism of the P and SH wave determined by the joint inversion, and the waveform fitting.

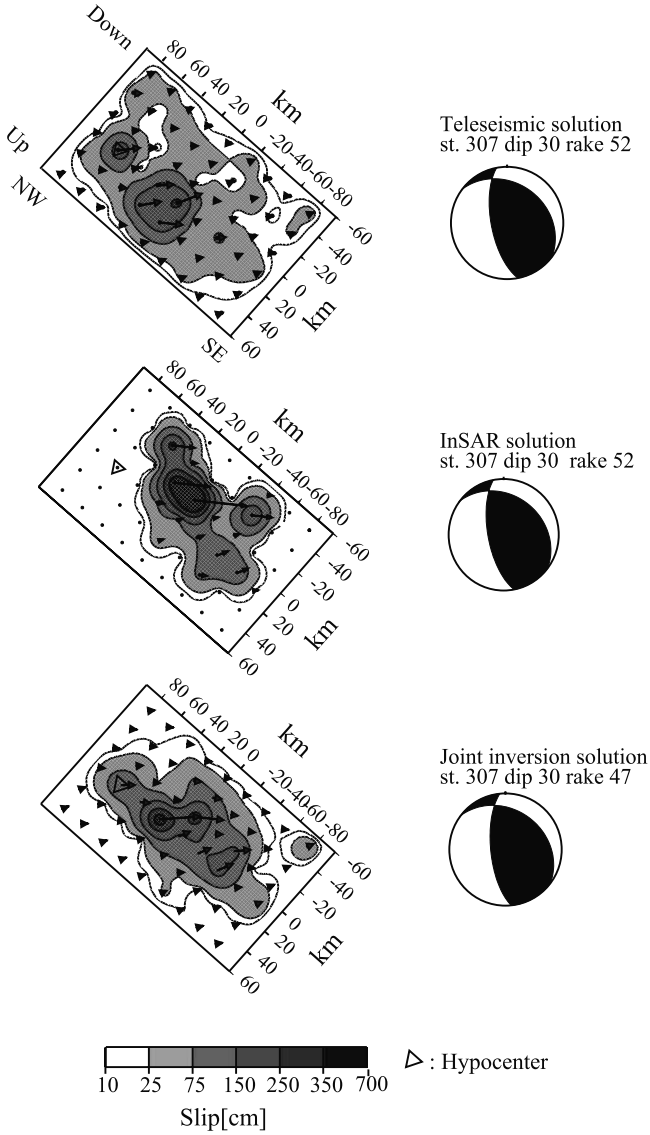

Figure 11. Slip maps from the separate and joint inversions of the real data. Also shown is their corresponding average focal mechanism. The arrows whose size is proportional to slip indicate the underthrusting direction. Hypocenter is indicated by a triangle.

elevation profiles of the coastal cordillera and of the marine terraces reflect the cumulative effects of the repetition of earthquakes similar to the 1996 event as suggested by *Swenson and Beck* [1999]. We note that the complexity of the earthquake source produces variable uplift along the coastal cordillera. Recurrent events may change the uplift pattern except if the source geometry is determined by the shape of the subducted Nazca ridge. It is therefore difficult to estimate a reliable coseismic uplift rate since we have access only to the slip map of a single event. Further,

Table 3. Misfit Values and Scalar Seismic Moment Resulting From the Inversions of the Actual Data[a]

	Teleseismic	InSAR	Joint
RMS teleseismic data	0.51	-	0.57
RMS InSAR data	-	0.09	0.14
Moment (10^{20} N m)	4.14	4.1	4.4

[a]Harvard moment = 4.57×10^{20} N m.

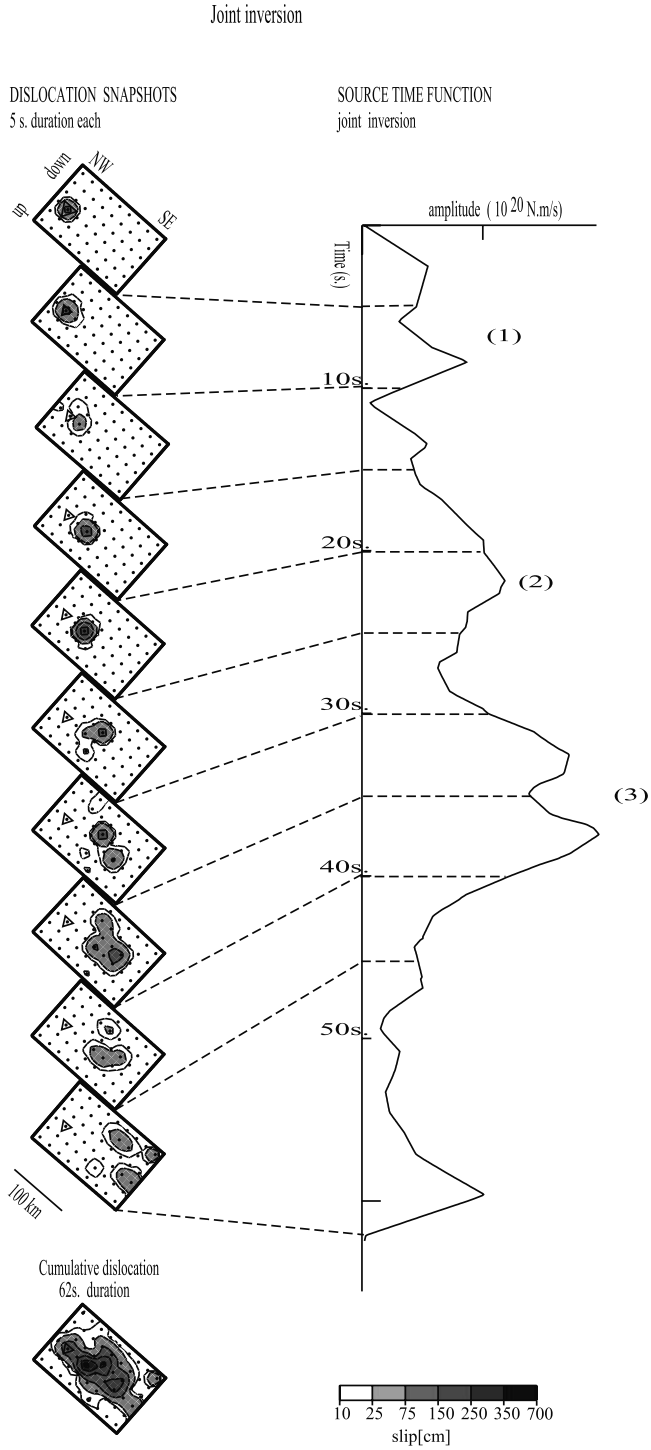

Figure 12. Source time function (right) and snapshots of the rupture history (left) for the 1996 Peru earthquake obtained with the joint inversion. Snapshots display cumulative slip in successive 5 s long time windows. Hypocenter is indicated by the triangle. (1), (2) and (3) indicate the three main pulses of moment release.

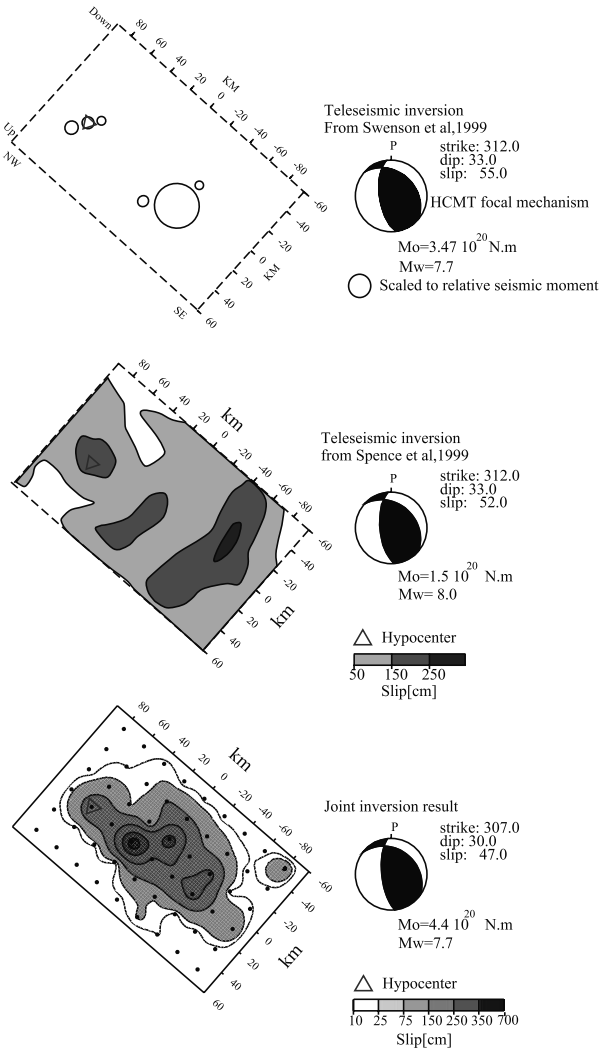

Figure 13. Solutions for the rupture of the 1996 Peru earthquake given by different studies. *Swenson and Beck* [1999] used an iterative, multistation, pulse stripping method [*Kikuchi and Kanamori*, 1982; *Kikuchi and Fukao*, 1985] which locates the maxima of energy release on the fault plane. *Spence et al.* [1999] performed a teleseismic inversion for the slip history base on a multitime window method [*Hartzell and Heaton*, 1983, 1986; *Hartzell and Langer*, 1993]. The dashed rectangle corresponds to the area of our fault model. Also shown is the respective focal mechanism for each inversion.

additional informations about the deformation field occurring in the interseismic period, which generally involves coastal subsidence, would be required to give an average return period for those earthquakes and to confirm their characteristic behavior.

9. Conclusion

[24] We observed that accurate slip map can be obtained from the joint inversion of remote access data which constrain both the timing of the rupture (teleseismic waveforms) and its spatial distribution (teleseismic + InSAR data). We show that the joint inversion of InSAR and teleseismic data resolve: 1) the location of the main asperities over the entire fault plane, despite the incomplete coverage of the surface displacement from the InSAR data and 2) the main characteristics of rupture timing. The southeastern and central parts of the rupture plane are essentially resolved by the InSAR data, and the northwestern part by the teleseismic data. The teleseismic data alone do not retrieve the same source model constrained with the addition of InSAR data. We show that synthetic tests are essential to understand the imaging power of individual data sets. The 1996 event (Mo = 4.4 $\times$ 10^{20} N m) ruptured the subduction interface on the southern flank of the Nazca ridge, as did the former Mw = 8.2, 1942 earthquake. It propagated unilateraly toward the SE, the main asperity

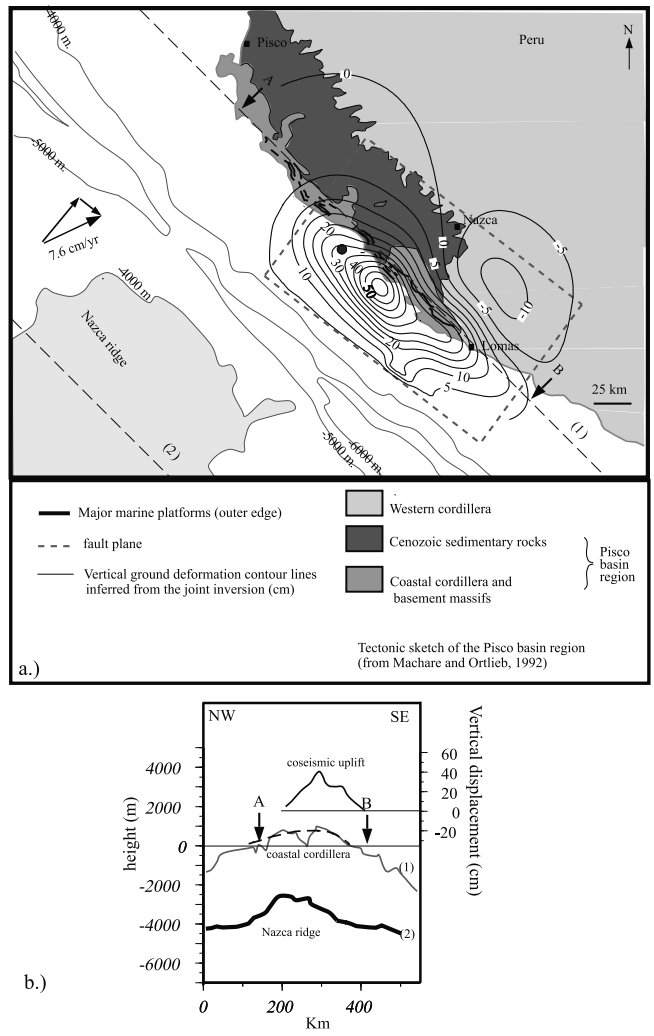

Figure 14. (a.) Tectonic sketch of the Pisco basin region and final vertical ground displacement (centimeters) inferred from the joint inversion results (thin contour lines). The dashed rectangle corresponds to the surface projection of the fault plane. (1) and (2) are two cross sections. (b.) Elevation profile across the coastal cordillera (1) its corresponding vertical coseismic uplift, and bathymetric profile(2) of the Nazca ridge. The finite deformation as figured by elevation of highest late cenozoic marine surfaces is shown by the dotted curve [*Machare and Ortlieb*, 1992].

being located 50 km away from the hypocenter. The slip area extended for more than 100 km in total, and mostly between 20 and 40 km depth. The similarity between coseismic uplift, topography of the coastal cordillera, and marine terraces suggests that coastal deformation may be related to the repetition of events similar to the 1996 earthquake.

[25] **Acknowledgments.** This work was supported by ESA (Contract ERS-A03-194) and ETH zürich. Part of this work was carried out at the Jet Propulsion Laboratory, California Institute of Technology, under contract with the National Aeronautics and Space Administration (NASA). We express our gratitude to P. Briole, D. Wald, and H. Lyon-Caen for reviewing the manuscript. Figures have been generated using the Generic Mapping Tools (http://gmt.soest.hawaii.edu/). Topographic and bathymetric data were available through the web site: http://topex.ucsd.edu/marine_topo/mar_topo.html. This is a publication 1268 of the Institute of Geophysics, ETHZ.

References

Chatelain, J. L., B. Guillier, P. Gueguen, and F. Bondoux, The Mw = 7.7 Nazca (Peru) earthquake, November 12, 1996: A repetition of the 1942 event?, *Seismol. Res. Lett.*, *68*, 917–922, 1997.

Costantini, M., A novel phase unwrapping method based on network progrmming, *IEEE Trans. Geosci. Remote Sens.*, *36*(3), 1998.

Delouis, B., P. Lundgren, J. Salichon, and D. Giardini, Joint inversion of InSAR and teleseismic data for the slip history of the 1999 Izmit (Turkey) earthquake, *Geophys. Res. Lett.*, *27*, 3389–3392, 2000.

Delouis, B., D. Giardini, P. Lundgren, and J. Salichon, Joint inversion of InSAR, teleseismic and strong motion data for the spatial and temporal distribution of earthquake slip: Application to the 1999 Izmit mainshock, *Bull. Seismol. Soc.*, *92*, in press, 2002.

Dorbath, L., A. Cisternas, and C. Dorbath, Assessment of the size of large and great historical earthquakes in Peru, *Bull. Seismol. Soc. Am.*, *80*, 551–576, 1990.

Hartzell, S., and T. H. Heaton, Inversion of strong ground motion and teleseismic wave form data for the fault rupture history of the 1979, Imperial Valley California, earthquake, *Bull. Seismol. Soc. Am.*, *73*, 1553–1583, 1983.

Hartzell, S., and T. H. Heaton, Rupture history of the Morgan Hill, California, earthquake from the inversion of strong motion records, *Bull. Seismol. Soc. Am.*, *76*, 649–674, 1986.

Hartzell, S., and C. Langer, Importance of model parametrization in finite fault inversion: Application to the 1974 Mw = 8.1 Peru earthquake, *J. Geophys. Res.*, *98*, 22,123–22,134, 1993.

Hernandez, B., F. Cotton, and M. Campillo, Contribution of radar interferometry to a two-step inversion of the kinematic process of the 1992 Landers earthquake, *J. Geophys. Res.*, *104*, 13,083–13,099, 1999.

Hsu, J. T., Quaternary uplift of the Peruvian coast related to the subduction of the Nazca ridge: 13.5 to 15.6 degrees south latitude, *Quat. Int.*, *15/61*, 87–97, 1992.

Kelleher, J. A., Rupture zone of large South American earthquakes and some predictions, *J. Geophys. Res.*, *77*, 2087–2103, 1972.

Kikuchi, M., and Y. Fukao, Iterative deconvolution of complex body waves from great earthquakes—The Tokachi-oki earthquake of 1968, *Phys. Earth Planet. Inter.*, *37*, 235–248, 1985.

Kikuchi, M., and H. Kanamori, Inversion of complex bodywaves, *Bull. Seismol. Soc. Am.*, *72*, 491–506, 1982.

Machare, J., and L. Ortlieb, Plio-quaternary vertical motions and the subduction of the Nazca ridge, central coast of Peru, *Tectonophysics*, *205*, 97–108, 1992.

Marshall, J. S., and R. S. Anderson, Quaternary uplift and seismic cycle deformation, peninsula de Nicoya, *Geol. Soc. Am. Bull.*, *107*, 463–473, 1995.

Nabelek, J., Determination of earthquake fault parameters from inversion of bodywaves, Ph.D. thesis, 361 pp., MIT, Cambridge, Mass., 1984.

Ocola, L., F. Monge, P. Huaco, and C. Aguero, Severidad de sacudimiento del sismo de Nazca de 1996, Taller de Trabajo Sismo de Nazca del 12 Noviembre de 1996, 6–7 Marzo de 1997, Lima, Peru, 1997.

Savage, J. C., Dislocations in seismology, in *Dislocations in Solids*, edited by F. R. N. Navarro, North-Holland, New York, 1980.

Spence, W., E. Mendoza, E. R. Engdahl, G. L. Choy, and E. Norabuena, Seismic subduction of the Nazca ridge as shown by the 1996–1997 Peru earthquakes, *Pure Appl. Geophys.*, *154*, 753–776, 1999.

Swenson, J. L., and S. L. Beck, Source characteristics of the November 12 1996 Mw = 7.7 Peru subduction zone earthquake, *Pure Appl. Geophys.*, *154*, 731–751, 1999.

Wald, D. J., and T. H. Heaton, Spatial and temporal distribution of slip for the 1992 Landers, California, earthquake, *Bull. Seismol. Soc. Am.*, *84*, 668–691, 1994.

Wright, T. J., B. E. Parsons, J. A. Jackson, M. Haynes, E. J. Fielding, P. C. England, and P. J. Clarke, Source parameters of the 1 October 1995 Dinar (Turkey) earthquake from SAR interferometry and seismic bodywave modeling, *Earth. Planet. Sci. Lett.*, *172*, 23–37, 1999.

M. Costantini, Telespazio, Rome, Italy.

B. Delouis, Geosciences Azur, CNRS/UNSA, Nice-Sophia Antipolis, France.

D. Giardini and J. Salichon, Institute of Geophysics, Eidgenossische Technische Hochschule, Zurich, Switzerland. (jerome@seismo.ifg.ethz.ch)

P. Lundgren and P. Rosen, Jet Propulsion Laboratory, Pasadena, CA, USA.